Journal of
Mechanical
Science and
Technology

Journal of Mechanical Science and Technology 21 (2007) 1869~1875

Unsteady flow and diaphragm motion in total artificial heart

X. L. Yang[1,2], Y. Liu[2,*] and J. M. Yang[1]

[1]*Department of Modern Mechanics, University of Science and Technology of China, Hefei, Anhui, 230027, China*
[2]*Department of Mechanical Engineering, The Hong Kong Polytechnic University, Hung Hom, Kowloon, Hong Kong*

(Manuscript Received May 7, 2007; Revised August 7, 2007; Accepted August 7, 2007)

Abstract

Unsteady flow and diaphragm motion in the phoenix artificial heart were studied using a CFD solver combined with an in-house developed FEM code. In diastole, the initially egg-shaped diaphragm deflates and forms two large depressions on the two sides and a small one on the round part. Vortices form in the blood chamber. In systole, the diaphragm inflates and pushes the blood to flow out through the opened outlet. The wall shear stress distribution is also strongly dependent on the flow field as well as the diaphragm motion.

Keywords: TAH; Simulation; Fluid-structure interation

1. Introduction

Total Artificial Heart (TAH) and Ventricular Assist Device (VAD) have been used in clinics being a bridge to transplant or a permanent substitute [1, 2] however, there are many disadvantages that restrain the wide application of TAH and VAD, such as infection, bleeding, thromboembolism, hemolysis, etc. [3-5]. Some of these complications are related strongly to the flow dynamics in an artificial heart, such as flow separation, recirculation, stagnation, high wall shear stress, high turbulent Reynolds stress, etc. One approach to tackling these problems in close proximity is to develop an understanding of the interaction of fluid and diaphragm. The basic physics of this problem could be gleaned from the flow pattern and shear stress distribution within the chamber.

Experimental investigations of fluid-structure interaction in push-plate type and sac type artificial hearts have been performed by many researchers [6-9]. They used different instruments, such as single channel pulsed ultrasonic velocimeter, Laser Doppler Anemometry (LDA) and Particle Image Velocimetry (PIV), to measure the instantaneous flow field, the wall shear stress and the Reynolds stresses. Generally, their results showed that the blood flow could provide good wash-out on the walls, but in some regions, there exist recirculations which may cause thrombus formation, and the shear stress near the valves is larger than that in the blood chamber.

The centrally-actuated type phoenix artificial heart was successfully applied in clinical cases [1, 10], but the studies on the flow phenomena in the blood chamber are quite limited. Lu et al. [10] investigated the flow in a centrally-actuated phoenix artificial heart using both flow visualization and a 2D LDA and found that the diaphragm within the blood chamber induced vortices that provided good wash-out on the inner walls. The Reynolds stress near the valves is greater than that inside the blood chamber. Although it is not very high, it may damage the blood cells if turbulence length scales and exposure time are taken into account.

Computational Fluid Dynamics (CFD) has been an alternatively aided tool to artificial organ design [11].

*Corresponding author. Tel.: +852 2766 7814, Fax.: +852 2365 4703
E-mail address: mmyliu@polyu.edu.hk

Several researchers carried out numerical simulation on different artificial hearts. Kiris et al. [12] and Konig et al. [13] simulated the unsteady flow in three-dimensional artificial heart models with moving boundary technique. In their studies, the diaphragm was modeled as a rigid piston and the main flow features were comparable to the experimental results. To actually simulate the diaphragm motion, some studies involved the interaction of the diaphragm and fluid [14-16], where large deformation of the diaphragm is coupled with the fluid flow.

In present study, the unsteady flow in the phoenix, a centrally-actuated type artificial heart, is investigated numerically. The fully three-dimensional incompressible laminar Navier-Stokes equations with moving grids are solved by using a commercial CFD solver FLUENT on unstructured tetrahedral meshes, and the motion of the diaphragm is modeled through an invoked self-developed FEM code. The objective is to study the fully coupled fluid-structure interaction between the fluid and the diaphragm and provide valuable information on artificial heart design.

2. Numerical modeling

2.1 Geometry of the model

A schematic view of the artificial heart model is shown in Fig. 1.

The pneumatically driven artificial heart is comprised of an outer rigid shell, an inner egg-shaped deformable diaphragm, an inlet and an outlet [10]. The space between the outer shell and the inner diaphragm is the blood chamber which mainly stores blood. To focus on the fluid-diaphragm interaction, additionally, considering the valve leaflets have only a secondary effect on the blood flow in the chamber [17], the effect of the valves fitted on the inlet and outlet is neglected and the inlet and outlet tubes are elongated to reduce the effect of the boundary condition on the inner flow. The diameters of the inlet tube and outlet tube are 3.0 cm and 2.5 cm, respectively. A simple on/off boundary condition [13, 15] is adopted both on inlet and outlet; namely, in diastole, the diaphragm shrinkage results in expansion of the blood chamber in size so that blood is inhaled through the opened inlet tube while the outlet is closed. In systole, the inlet is closed, and blood is pushed out via the opened outlet due to the inflation of the diaphragm.

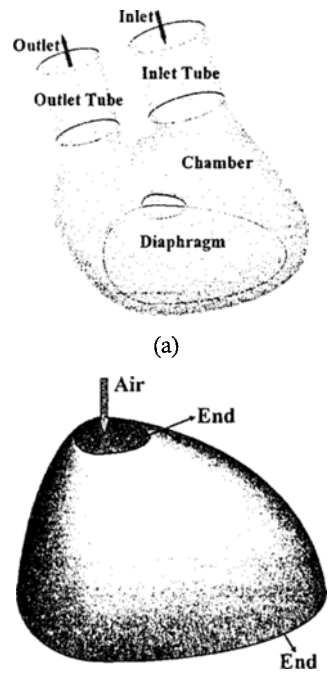

Fig. 1. (a) A schematic view of the artificial heart model; (b) The shape of the initially egg-shaped diaphragm.

2.2 Solid formulation

The governing equation of diaphragm deformation is

$$\rho_s \ddot{u}_i = \sigma_{ij,j} \text{, within the body} \quad (1)$$

$$\sigma_{ij} n_j = \bar{t}_i \text{, on boundaries} \quad (2)$$

where u is the displacement, σ_{ij} is the ij^{th} component of the Cauchy stress tensor, ρ_s is the density of the solid, $\ddot{u}_i$ indicates the acceleration of the material particle in the coordinate i direction, n_j is the outward normal vector and $\bar{t}_i$ is the externally exerted force (the transmural pressure) on boundaries. The governing equations, Eqs. (1) and (2) are used to construct the incremental form of Updated Lagrangian (U.L.) formulation by using the virtual displacements principle and solved by an in-house developed FEM code using the Newmark implicit method. The diaphragm is discretized by a hybrid strain based 3-node flat triangular shell element which is capable of reflecting the true normal rotations and desirable bending and membrane behaviors [18], and the total element number is 2644. The thickness of the

diaphragm is 0.5 mm. Although the diaphragm experiences large deformation, its strain is usually small; therefore it is considered as elastic medium whose density is 1.5×10^3 kg/m^3 and Young's module is 1.0×10^9 Pa. The Poisson ratio is selected as 0.49, which represents the nearly-incompressible material.

2.3 Fluid formulation

The flow field is solved by the ALE formulation of Navier-Stokes equations

$$\frac{\partial \vec{u}}{\partial t} + (\vec{u} - \vec{u}_g)\cdot\nabla\vec{u} = -\frac{1}{\rho}\nabla p + \nu\nabla^2\vec{u} \tag{3}$$

and the continuity equation

$$\nabla\cdot\vec{u} = 0 \tag{4}$$

where $\vec{u}$ is the velocity of the fluid, $\vec{u}_g$ the velocity of the grid, ρ the density, p the pressure and ν the kinematic viscosity of the fluid. In large vessels such as the heart and aorta, the blood can be considered as a Newtonian fluid, whose density and viscosity are 1050 kg/m^3 and 0.004 kg/m·s, respectively [19]. The fluid domain is discretized by 178630 unstructured tetrahedral cells. These numbers are determined by using different meshes, from coarse to progressively fine, until the calculated mass flow rates are mesh-convergent to within a prescribed tolerance (~ 3.0%). The fluid flow is solved by CFD solver, FLUENT (6.1.22).

2.4 Solid-fluid interaction and boundary and initial conditions

During calculation, a transmural pressure (the blood pressure minus the air pressure), which is sinusoidal with time but uniform in space, is applied on the diaphragm. The transmural pressure is

$$\Delta p = -C\sin(2\pi t/T) \tag{5}$$

where T is the period of the artificial heart, C is an adjustable factor which is chosen discreetly to make the diaphragm deform sufficiently, but it does not contact at any time.

At the beginning of every time step, the FEM code is invoked to solve the deformation of the diaphragm, the computational domain of the fluid deforms according to the displacement of the diaphragm and the attached grids are updated by using the spring-based smoothing method, and then the flow field is calculated.

At the two ends of the diaphragm [shown in Fig. 1(b)], the clamped boundary condition is applied, namely,

$$u = v = w = \theta_x = \theta_y = \theta_z = 0 \tag{6}$$

where u, v, w and θ_x, θ_y, θ_z are the translation and rotation displacements of x, y, z direction, respectively.

A no-slip boundary condition is applied on all walls, namely, on the stationary walls, velocity is zero and on the diaphragm, the velocity of fluid is as same as that of the diaphragm.

At the beginning, the velocity and pressure of the blood, the velocity and acceleration of the diaphragm are all set to zero. Calculations are performed for several periods and stopped until stationary solutions are obtained.

2.5 Validation of solid boundary deformation

The validity of the proposed FEM code for diaphragm deformation is examined by a benchmark problem [19, 20], where a concentrated dynamic load exerts on the central node of a hinged cylindrical shell, as shown in Fig. 2. Due to symmetry, only a quarter of the cylindrical shell is considered. The geometry, boundary conditions, material properties and load history are all shown in Fig. 2.

Variable time step sizes are used to ensure an accurate and stable solution, i.e., 10^{-4} s in the pre-buckling region and 2×10^{-5} s in the buckling and post-buckling regions. From Fig. 2, it is clear that the present calculations and the results reported earlier [20, 21] are consistent.

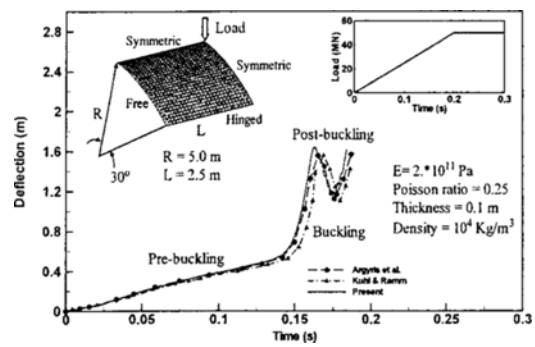

Fig. 2. A comparison of the deflection of the central node in the benchmark problem.

3. Results and discussion

In calculation, the mean Reynolds number is defined as [22]

$$Re = \frac{UD}{\nu} = \frac{4\Delta V}{\pi \nu DT} \tag{7}$$

where, ΔV is the stroke volume, T the diastolic duration and D the diameter of the inlet tube. The heart beat rate is set as 75 beats per minute (bpm) and the diastolic stage experiences 50% of the whole period. The stroke volume of the artificial heart model is about 46.7 ml; therefore, Re = 1300. The mean Re being not very high indicates the main flow may be considered as laminar. However, as indicated by Konig et al. [13], the effect of the valves and the sudden expansion of the flow as it enters the blood chamber will cause turbulent flow. Because it is difficult to deal with the possibility of intermittent turbulent flow, the simulation in present study is based upon a laminar solution.

3.1 Motion of the diaphragm

The deformation of the diaphragm is a significant feature of TAH which may determine the flow patterns in the chamber. The instantaneous shapes of the diaphragm with an interval time of 0.1 in diastole are shown in Fig. 3, where the period has been normalized to unity.

It can be seen that, at t = 0.1, the deformation is very small. Until the middle stage, two large depressions can be seen on the upper and lower sides. At t = 0.4, a small depression appears clearly on the round part of the diaphragm. The diaphragm shrinks further and the three depressions become larger and larger until the diastole ends (t = 0.5). As observed in the experiment of Lu et al. [10], the originally egg-shaped diaphragm folds into a scalene triangle-shaped configuration. The deformation of the diaphragm enlarges the domain of the blood chamber so that the blood can be induced into the artificial heart.

Fig. 4 shows the mass flow rate at inlet, which could reflect the deformation of the diaphragm from another view. It can be seen that in the early stage, the mass flow is very small. At t = 0.15, the mass flow begins to increase dramatically, until t = 0.25 where the increment becomes slow, and at t = 0.3, it becomes steep again. At t = 0.35, the mass flow rate reaches its peak value, then it decreases quickly until t = 0.5 where the mass flow rate becomes zero due to the inlet closure. In the systole, the diaphragm inflates to its original shape approximately along the same path.

3.2 Flow vectors

The fluid dynamic characteristics of the TAH could be gleaned from the flow vectors within the chamber. Fig. 5 shows the instantaneous flow vectors on the plane which crosses through the centerlines of the inlet and outlet. In the early and middle stage of diastole, the deformation of the diaphragm induces large velocities in the inlet tube and the right part of the blood chamber, but elsewhere the velocity has no discernable change. In the later stage of diastole, the deformation of the diaphragm becomes smaller so that the blood velocity in the inlet tube becomes weak. A notable phenomenon is that, at the end of the inlet tube, the boundary layer separates. This is due to the Bernoulli Effect, i.e., the fluid decelerates when it passes expansion passage and the pressure increases. In addition, the deceleration due to the unsteadiness also makes the pressure increase. When the inverse

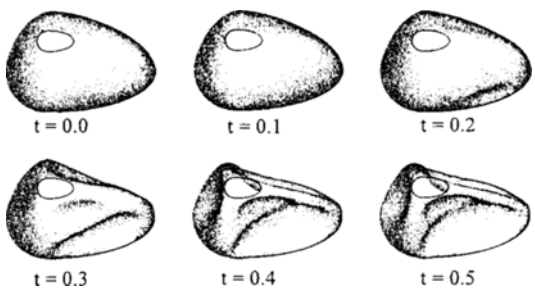

Fig. 3. The instantaneous configurations of the diaphragm in diastole.

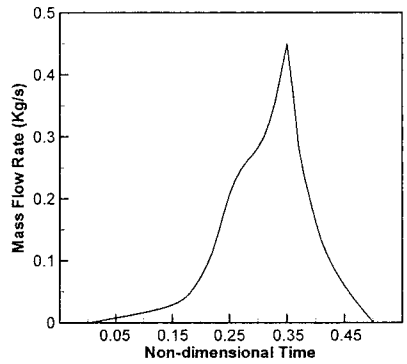

Fig. 4. The mass flow rate of the inlet in diastole.

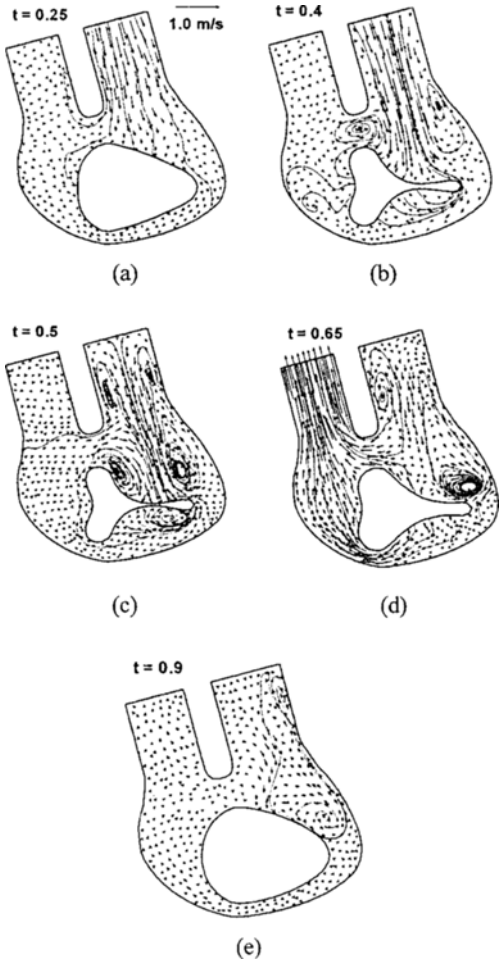

Fig. 5. The instantaneous flow vectors.

pressure gradient is large enough, the boundary layer begins to separate. The shed boundary layer forms two vortices as indicated in Fig. 5(b). These two vortices travel downwards into the upper depression of the diaphragm as shown in Fig. 5(c). At the end of diastole, a pair of small vortices can also be found in the inlet tube. It is mostly attributed to the fluid deceleration and the inlet closure. Moreover, another vortex can be found in the lower depression of the diaphragm. In the systolic period, the diaphragm inflates and the blood is pushed out from the blood chamber via the opened outlet. It goes without saying that the velocity in the outlet tube will increase. As shown in Fig. 5(d), at t = 0.65, the flow velocity in the outlet tube and the left part of the blood chamber increases significantly. A large vortex, which comes from the separation of the boundary layer, can be found in the right part of the blood chamber. Moreover, the pair of small vortices remains in the inlet tube and their intensities have become much smaller. At t = 0.9, the diaphragm almost reaches its original shape; therefore, its deformation is very small. Consequently, the velocity of the blood in the outlet tube becomes very weak. The vortex in the right part of the blood chamber is also very weak but it is still discernable.

3.3 Wall shear stresses

Wall shear stress plays an important role in thromboembolism and hemolysis. It is well known that high wall shear stress may damage the blood cells and activate the platelets. The released protein can clot together and form thrombus. Therefore, high wall shear stress should be avoided, and understanding the physics of the wall shear stress is crucial to artificial heart design.

The wall shear stress distributions on the outer walls (including the outer shell, the inlet tube wall and the outlet tube wall) and diaphragm are depicted in Fig. 6. At the early of diastole t = 0.1, the wall shear stresses are weak on the outer walls and the diaphragm. With the development of the flow field in the inlet tube, the wall shear stress on the inlet tube wall increases gradually. On the ridges of the diaphragm, the wall shear stress also increases. The most likely explanation is that the distance between the ridges and the outer walls becomes narrow so that the velocity gradient becomes larger. When the fluid in the inlet tube begins to decelerate, the wall shear stress does not increase anymore. On the outer walls, the high wall shear stress zone expands downwards. In the systole, increasing velocity gradient leads to high wall shear stress on the outlet tube wall. The largest wall shear stress occurs at t = 0.65. It is not surprising because at this moment the flow rate of the outlet is the largest. Additionally, on the outer walls, at the regions which are near the ridges of the diaphragm, larger wall shear stress can be observed. Also, on the ridges of the diaphragm, the wall shear stress is large. In the later stage, the wall shear stress decreases due to the deceleration of the fluid velocity.

The largest wall shear stress is generated at the conjunction of the outlet tube and the blood chamber in the middle of systole. If the effect of valve is also considered, the wall shear stress will become even larger and the blood cell may be damaged and platelet may be activated here.

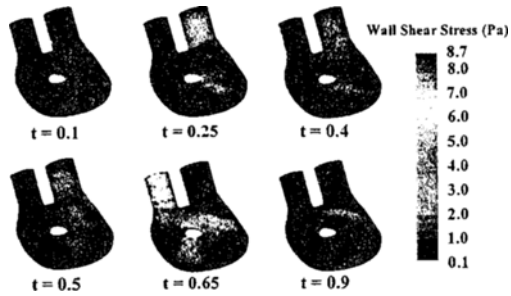

(a)

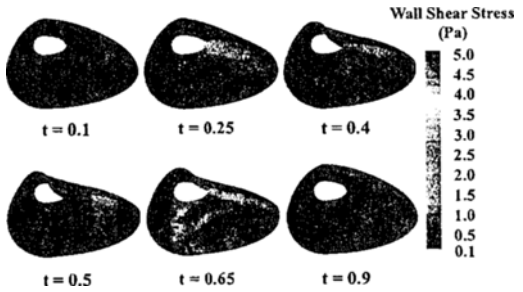

(b)

Fig. 6. The distributions of wall shear stresses on (a) outer walls; (b) diaphragm.

4. Conclusion

The motion of the diaphragm and the induced unsteady flow in a centrally-actuated artificial heart are simulated by using a CFD solver combined with an FEM code which is used to solve structural deformation. The calculated results lead to the following conclusions:

(1) The originally egg-shaped thin diaphragm shrinks and folds into scalene triangle-shaped configuration in diastole.

(2) In the middle of diastole, vortices form in the blood chamber due to the boundary layer separation. In the later stage, a weak vortex forms in the lower depression of the diaphragm and two small vortices form in the inlet tube.

(3) Large wall shear stress occurs on the inlet tube wall in diastole and outlet tube wall in systole. The largest wall shear stress occurs on the outlet tube wall at the moment when the mass flow of outlet is largest. The higher wall shear stress also occurs on the ridges of diaphragm and the relevant regions of blood chamber.

Acknowledgement

A model of the Phoenix Artificial Heart was provided by Dr. Kevin K.T. Cheng under the assistance of Prof. Ronald M.C. So. Funding support was given by the Research Grants Council of the Government of the HKSAR under Grant No. PolyU 5273/04E and by the Hong Kong Polytechnic University under CRG No. A-PG08. These supports are gratefully acknowledged.

Nomenclature

D : Diameter of the inlet tube, m
n : Outward normal vector
p : Pressure of fluid, Pa
t : Time, s
$\bar{t}$: Externally exerted force, N
T : The diastolic duration or the whole period of the artificial heart, s
u : Displacement of the structure, m
$\bar{u}$: Velocity vectors of the fluid and grid, m/s
$\ddot{u}$: Acceleration of the material particle, m/s^2
σ : Cauchy stress tensor, Pa
ρ : Densities of the solid and fluid, kg/m^3
ν : Kinematic viscosity of the fluid, m^2/s

Subscripts

g : Grid
i : Coordinate i direction
s : Solid

References

[1] J. Wei, K. K. Cheng, D. Y. Tung, C. Y. Chang, W. M. Wan and Y. C. Chuang, Successful use of Phoenix-7 total artificial heart, *Transplantation Proceedings.* 30 (1998) 3403-3404.

[2] D. A. Cooley, The total artificial heart, *Nat. Med.* 9 (2003) 108-111.

[3] B. G. Min and K. Sun, The total artificial heart and implantable biventricular assist device, *J. Artif. Organs.* 5 (2002) 147-148.

[4] H. Matsuda and G. Matsumiya, Current status of left ventricular assist devices: the role in bridge to heart transplantation and future perspectives, *J. Artif. Organs.* 6 (2003) 157-161.

[5] O. H. Frazier, R. D. Dowling, L. A. Gray, N. A. Shah, T. Pool and I. Gregoric, The total artificial heart: where we stand, *Cardiology.* 101 (2004) 117-

121.

[6] J. M. Tarbell, J. P. Gunshinan, D. B. Geselowitz, G. Rosenberg, K. K. Shung and W. S. Pierce, Pulsed ultrasonic doppler velocity measurements inside a left ventricular assist device, *ASME J. Biomech. Engrg.* 108 (1986) 232-238.

[7] W. Jin and C. Clark, Experimental investigation of unsteady flow behaviour within a sac-type ventricular assist device (VAD), *J. Biomech.* 26 (1993) 697-707.

[8] J. T. Baldwin, S. Deutsch, D. B. Geselowitz and J. M. Tarbell, LDA measurements of mean velocity and Reynolds stress fields within an artificial heart ventricle, *ASME J. Biomech. Engrg.* 116 (1994) 190-200.

[9] P. Hochareon, K. B. Manning, A. A. Fontaine, J. M. Tarbell and S. Deutsch, Fluid dynamic analysis of the 50 cc Penn State artificial heart under physiological operating conditions using particle image velocimetry, *ASME J. Biomech. Engrg.* 126 (2004) 585-593.

[10] P. C. Lu, J. S. Liu, C. S. Tung, K. K. T. Cheng and J. Wei, An investigation of the flow within the phoenix artificial heart, *Biomed. Eng. Appl. Basis. Comm.* 11 (1999) 277-284.

[11] P. Verdonck, The role of computational fluid dynamics for artificial organ design, *Artif. Organs.* 26 (2002) 569-570.

[12] C. Kiris, D. Kwak, S. Rogers and I. D. Chang, Computational approach for probing the flow through artificial heart devices, *ASME J. Biomech. Engrg.* 119 (1997) 452-459.

[13] C. S. Konig, C. Clark and M. R. Mokhtarzadeh-Dehghan, Investigation of unsteady flow in a model of a ventricular assist device by numerical modelling and comparison with experiment, *Med. Engrg. Phys.* 21 (1999) 53-64.

[14] Q. Zhang and T. Hisada, Analysis of fluid-structure interaction problems with structural buckling and large domain changes by ALE finite element method, *Comp. Methods Appl. Mech. Engrg.* 190 (2001) 6341-6357.

[15] E. B. Shim, J. Y. Yeo, H. J. Ko, C. H. Youn, Y. R. Lee, C. Y. Park, B. G. Min and K. Sun, Numerical analysis of the three-dimensional blood flow in the Korean artificial heart, *Artif. Organs* 27 (2003) 49-60.

[16] M. G. Doyle, Simulation of blood flow in a ventricular assistant device with fluid-structure interaction effects, Thesis, University of Ottawa, Ottawa, Canada, (2004)

[17] M. Rosenfeld, I. Avrahami and S. Einav, Unsteady effects on the flow across tilting disk valves. *ASME J. Biomech. Engrg.* 124 (2002) 21-29.

[18] M. L. Liu and C. W. S. To, Hybrid strain based three-node flat triangular shell elements - I. Nonlinear theory and incremental formulation, *Comput. Struct.* 54 (1995) 1031-1056.

[19] T. J. Pedley, The fluid mechanics of large blood vessels, Cambridge University Press, (1980).

[20] D. Kuhl and E. Ramm, Generalized energy-momentum method for non-linear adaptive shell dynamics, *Comp. Methods Appl. Mech. Engrg.* 178 (1999) 343-366.

[21] J. Argyris, M. Papadrakakis and Z. S. Mouroutis, Nonlinear dynamic analysis of shells with the triangular element TRIC, *Comp. Methods Appl. Mech. Engrg.* 192 (2003) 3005-3038.

[22] C. Bachmann, G. Hugo, G. Rosenberg, S. Deutsch, A. Frontaine and J. M. Tarbell, Fluid dynamics of a pediatric ventricular assist device, *Artif. Organs.* 24 (2000) 362-372.